Journal of Magnetic Resonance 305 (2019) 152–161

Contents lists available at ScienceDirect

Journal of Magnetic Resonance

journal homepage: www.elsevier.com/locate/jmr

Effects of motion on MRI signal decay from micron-scale particles

Daniel D. Borup *, Christopher J. Elkins, John K. Eaton

Department of Mechanical Engineering, 488 Escondido Mall, Building 500, Stanford, CA 94305, USA

ARTICLE INFO

Article history:
Received 25 February 2019
Revised 25 June 2019
Accepted 26 June 2019
Available online 28 June 2019

Keywords:
Magnetic resonance imaging
Turbulence
Flow
Signal decay
Particles

ABSTRACT

Transverse decay rate (R2*) mapping is an established method for measuring iron overload in various biological tissues. Recently, R2* mapping was used to measure the mean 3D concentration distribution of micron-size particles dispersed in turbulent flows. However, some discrepancy was observed between the measured R2* and the expected decay based on existing theory. The present paper examines three flow-related mechanisms that could be responsible for this discrepancy. Computational simulations were used to study the effects of relative particle-fluid motion and preferential concentration by turbulence, while the effect of enhanced proton dispersion due to turbulence was examined via the existing MRI relaxation theory. Each flow phenomenon was shown to produce a different effect on the signal-time curve, as well as the extracted R2*. Comparison to experimental data in a square channel flow showed that relative motion between the particles and fluid was the most likely cause of the discrepancy in the previous experiments; however, all three effects may be present in both medical and non-medical flows, and their differing effects on the MRI signal may eventually allow for their identification from MRI data.

1. Introduction

Mapping of transverse signal decay properties (T_2 or T_2^*) is a growing tool for identifying important diagnostic information in the medical arena [1]. Both decay properties can be used to identify iron overload or hemorrhage in liver, heart, and brain tissue [2], while T_2 mapping also is useful in detecting myocardial inflammation or ischemia [3]. More generally, the modification of transverse relaxation rate due to changes in magnetic susceptibility is the basis for BOLD imaging [4] and important in the function of superparamagnetic iron oxide (SPIO) contrast agents [5].

The effects of turbulent flow on MRI signal have also been examined over the past few decades. Early measurements provided quantitative maps of the eddy diffusivity in turbulent flows based on the signal decrease due to increasing levels of turbulence [6,7]. However, direct turbulence measurements are subject to large noise, frequently requiring a large number of averages [8]. The past few decades have seen advances in the reliability of MRI turbulence measurement and consideration of new effects [9], as part of an overall increase in research on advanced flow imaging techniques [10]. For this study, it is important to note that turbulence causes a decrease in signal which varies nonlinearly with the echo time, TE; thus, when considering the effects of particles in a turbulent flow, it will be important to normalize against measurements with similar levels of turbulence under particle-free conditions.

MRI is finding increasing application as a tool for studying complex engineering flows because fully 3D measurements can be made without optical access. Recent examples include studies of aircraft gas turbine engine components [11], porous media flows [12], and vertical-axis wind turbines [13]. When studying particle-laden flows, existing (non-MRI) experimental techniques are limited to pointwise measurements, which provide poor data coverage, and laser-based measurements, which impose severe restrictions on the flow geometry and maximum particle concentration. MRI relaxometry, in contrast, offers the opportunity to acquire a quantitative map of the mean 3D particle concentration field in flows of arbitrary geometric complexity and at high particle loading. Having the full 3D concentration field allows for unique analysis of complex particle transport patterns, and also allows for robust validation of computational flow simulations, which are still of limited accuracy in particle-laden flow systems.

A spherical micro- or nano-particle will create a local disturbance to a normally uniform magnetic field [14]. This disturbance creates variations in the local precession frequency for protons in a surrounding medium. Although these variations may affect T_1 and T_2, the present work is limited to the transverse effect in Spoiled Gradient-Recalled Echo (SPGR) sequences, which is governed by T_2^* and the associated decay *rate*, $R_2^* = 1/T_2^*$.

* Corresponding author at: Mayo Clinic Department of Radiology, 333 4th Ave SW, Rochester, MN 55902, USA.
E-mail address: borup.daniel@mayo.edu (D.D. Borup).

https://doi.org/10.1016/j.jmr.2019.06.014
1090-7807/

Describing the signal evolution for a medium containing a distribution of particles typically begins with its classification into one of two regimes based on the particle diameter, d_p, the diffusion coefficient of the surrounding medium, D, and an appropriate time scale over which decay occurs. The latter is taken to be the maximum TE [15]. In most cases the diffusion coefficient is assumed to be the self-diffusion coefficient of water, $D \approx 2 \times 10^{-9}$ m^2/s, so in practice the regime is set by d_p alone.

In the so-called "static dephasing regime" (SDR), water molecules diffuse over a short distance relative to the field disturbance pattern during the characteristic decay time. Each proton "feels" a near-constant frequency shift, so that protons in different locations lose phase coherence. The resulting effect is a decrease in the signal magnitude. In the SDR, the signal decay rate depends linearly on the particle volume fraction, ϕ_V, according to the following relationship [16,17]:

$$R^*_{2,part} = \frac{2\pi}{9\sqrt{3}} \omega_0 |\Delta\chi| \phi_V \tag{1}$$

where ω_0 is the Larmor frequency, and $|\Delta\chi|$ is the magnitude of the magnetic susceptibility difference between the particle and surrounding medium. Here the term $R^*_{2,part}$ is used to indicate that decay may occur due to other sources simultaneously; decay rate terms are understood to be additive. Eq. 1 has been published in numerous forms—the present formulation requires that $|\Delta\chi|$ be computed from volume susceptibility values in the SI units. If EMU values are used (as in [17]), the leading constant becomes $\frac{8\pi^2}{9\sqrt{3}}$.

At the opposite end of the spectrum is the "motional averaging regime" (MAR). In the MAR, a proton moves past many particles during the characteristic decay time, experiencing both increased and decreased frequencies relative to ω_0. This reduces the expected total phase shift for each proton, which in turn reduces the amount of dephasing across a voxel. Resulting R^*_2 values are lower in the MAR than the SDR for a given particle volume fraction, and governed by a different relationship [15,18]:

$$R^*_{2,part} = \frac{16}{405} \phi_V (\omega_0 |\Delta\chi|)^2 \tau_D \tag{2}$$

where $\tau_D = d_p^2/(4D)$ is a characteristic diffusion time based on the *particle size*.

The crossover between MAR and SDR lies at the value of τ_D that produces the same decay in Eqs. 1 and 2, which will be denoted the critical diffusion time:

$$\tau_{D,crit} = \frac{45\pi}{8\sqrt{3}\omega_0 |\Delta\chi|} \tag{3}$$

Since D is assumed constant, $\tau_{D,crit}$ implies a critical particle diameter delimiting the two regimes. However, this assumption may not prove well-founded in turbulent flows, as discussed later. The MAR and SDR also are not discrete regimes; Eqs. 1 and 2 are strictly accurate only for $\tau_D \gg \tau_{D,crit}$ and $\tau_D \ll \tau_{D,crit}$, respectively. Various descriptions have been advanced in an attempt to provide regime-independent predictions, including the two-site exchange model, inner- and outer-sphere relaxation theory, and mean gradient diffusion theory [18]. More recent developments include considering the effects of "restricted" diffusion [19], or mitigating the effects of noise on the extracted signal decay rate [20]. In addition, several studies have validated the theoretical predictions for the SDR, MAR, and transitional regimes using both experiment and simulation [21–23]. However, many potential flow-related effects remain unexplored in the literature, particularly for turbulent flows.

1.1. Flow effects

A critical dimensionless parameter in fluid mechanics is the Reynolds number, defined as:

$$Re = \frac{UL}{\nu} \tag{4}$$

where U and L are appropriate velocity and length scales for the flow, and ν is the fluid kinematic viscosity (10^{-6} m^2/s for water at 20 °C). For example, the Reynolds number of a square channel flow is obtained by substituting the channel height, H, and bulk (mean) velocity, U_{bulk}, for L and U in Eq. 4. The Reynolds number is more useful than dimensional quantities (e.g., the volumetric flow rate or mean velocity) in predicting the properties of a given flow, such as the presence of turbulence.

For particle-laden flows, an additional dimensionless parameter known as the Stokes number (Stk) is useful:

$$Stk = \frac{\tau_p}{\tau_f} \tag{5}$$

where τ_f is the fluid time scale, $\tau_f = L/U$, and τ_p is the particle aerodynamic time constant, defined as:

$$\tau_p = \frac{\rho_p d_p^2}{18 \rho_f \nu} \psi(Re_p) \tag{6}$$

where new parameters are the particle and fluid densities, ρ_p and ρ_f, respectively, and a correction function $\psi(Re_p)$ that depends only on the particle Reynolds number:

$$Re_p = \frac{U_{rel} d_p}{\nu} \tag{7}$$

The correction function $\psi(Re_p)$ is approximately 1 when $Re_p \leqslant 0.1$; an empirical approximation for the full function is available in [24]. A conservative estimate for the relative velocity, U_{rel}, is U_{bulk}.

Recent results show that R^*_2 mapping can yield reliable particle volume fraction measurements using a newly developed protocol referred to as MRP (Magnetic Resonance with Particles). MRP was previously applied to static gel suspensions of particles [25], as well as several turbulent flows [25–27]. All MRP experiments to date fell well within the SDR, as it is ordinarily defined: titanium microspheres with mean $d_p = 33$ μm were imaged in room-temperature water ($D = 2 \times 10^{-9}$ m^2/s), giving $\tau_D = 0.14$ s, which is well above $\tau_{D,crit} = 7 \times 10^{-5}$ s for the particle material ($|\Delta\chi| = 182 \times 10^{-6}$ in SI units) and Larmor frequency ($\omega_0 = 802$ Mrad/s at 3T). The results of these studies show that the SDR is an accurate model for $R^*_{2,part}$ in non-flowing systems and in some turbulent flows. However, the relationship between decay rate and particle concentration deviated from Eq. 1 in some portions of two of the three flows, suggesting that either the SDR model or the SDR/MAR classification is inadequate. The present work explores the discrepancy between measured and expected $R^*_{2,part}$ due to the effects of three physical processes common in particle-laden flows: preferential concentration of particles by turbulence, relative particle-fluid motion, and enhanced self-diffusion of water molecules due to turbulent mixing.

Turbulent eddies can cause particles to form dense clusters and sparse voids to a much higher degree than would be expected given a random particle distribution. This phenomenon, called "preferential concentration," depends on the smallest scales of the turbulence, which are known as the Kolmogorov microscales. In the present paper, the Stokes number will be defined by using the Kolmogorov time scale, τ_η, for τ_f in Eq. 5. Particles tend to preferentially concentrate in the range $0.1 < Stk < 10$, with peak intensity near $Stk = 1$. However, the characteristics of the particle clusters can vary markedly between flows, making this a difficult phenomenon to describe analytically.

The second phenomenon considered is uniform relative motion (often called "slip") between the particles and fluid. Few (if any) studies have considered the MR relaxation effects of non-diffusive relative motion between the particles and fluid. However, slip can occur in any flow—laminar or turbulent—either due to gravitational settling or particles deviating from the flow trajectory in regions of rapid fluid acceleration. The mean slip velocity increases for heavier or larger particles and in faster flows. Thus, while slip velocities may be small for nanoparticles or very slow flows, they often are non-negligible for micron-size particles in centimeter-size channels. Furthermore, even small slip velocities may be important for nanoparticles in MR relaxometry because the size of the magnetic field disturbance scales with d_p.

The final process examined is that by which chaotic fluid motion in a turbulent flow acts to mix fluid molecules much more quickly than molecular diffusion alone. The net effect is most commonly described in terms of an isotropic turbulent diffusion coefficient, D_t, which has the same units as D. Because D_t is usually orders of magnitude larger than D, molecular diffusion is ignored in most turbulent flows. The simplest means to consider the effects of turbulent dispersion within the existing dephasing models is to substitute an estimate of D_t for D. The expected effect would be a shift away from the SDR and towards the MAR for a given particle size and material due to faster diffusion of the protons. However, the apparent D_t as measured by MR has been shown to vary with echo time, increasing with TE for short values before eventually reaching a plateau [28]. This means that, for short-TE scans, the appropriate D_t may be difficult to estimate a priori.

The goal of the present paper is to broaden the physical understanding of particle-induced relaxation rate enhancement to include three flow-related phenomena not considered previously. Simulations and theory are employed to probe each process independently, since creating an experiment in which each effect is isolated is difficult or impossible. Two of these effects occur only in turbulent flows; turbulence dominates most technological and environmental flows, while in the medical arena it is present in the largest arteries and airways, behind flow obstructions including stenoses, heart valves, and the nasal valve, and around distorted flow paths such as aneurysms and obtuse bronchial bifurcations. Therefore, the present results may be relevant to a broad range of medical and non-medical applications.

2. Methods

2.1. Numerical simulations

A series of computational simulations was carried out to assess the effects of preferential concentration and particle-fluid slip. The simulation domain was representative of a triply periodic, $4 \times 4 \times 4$ cube of isotropic 1 mm^3 voxels. Simulations were performed with static particles in a random distribution (the baseline case), with preferentially concentrated particles ("Pref. Conc."), and with relative particle-fluid slip ("Slip"). Particle concentrations with preferential concentration were generated at three Stokes numbers based on a high-fidelity computational fluid dynamics (CFD) simulation [29]. Each point particle was assumed to produce a magnetic field disturbance equal to the theoretical effect for a titanium sphere with $d_p = 33$ µm. Simulations were carried out for five particle volume fractions: $\phi_V = 0.05\%$, 0.1%, 0.2%, 0.4%, and 0.8%. Table 1 lists the full parameter set for these three cases; further details of the computational method are included in the Appendix.

Table 1
Simulation variables and values examined.

Case	Particle locations	Slip velocity	Slip angle
Baseline	*Random*	0	*N/A*
Pref. conc.	*Stk* = 1/4, 1, 4	0	*N/A*
Slip	*Random*	0–46.8 mm/s	0–90°

2.2. Flow experiments

Experimental data in turbulent flow are reported from the calibration channel shown in Fig. 1. Full details are available in [25]. Imaging was performed using a clinical 3T scanner (GE Discovery 750, GE Healthcare, Waukesha, WI) and a standard single-channel transmit/receive head coil. The channel had a 15×15 mm square cross-section and was oriented vertically within the magnet bore, passing between two "bars" of the head coil. For a supine patient, Fig. 1 would correspond to a sagittal slice with y pointing in the posterior direction. Particles were supplied to the channel from a custom MR-compatible supply feeder placed just outside the MRI bore [26]. The particles were injected in a spray pattern at the channel centerline; the flow then passed through several rows of mixing pins (1.5 mm diameter, 3.75 mm centerline spacing) to produce a uniform particle concentration distribution across the channel cross-section with turbulent fluctuations on the order of 5% of the mean velocity.

Data were acquired using a fast, 3D, RF-spoiled gradient echo sequence known as mFast. The signal was obtained at three echo times, with a separate excitation for each echo at each line of k-space. The following imaging parameters were used: TR = 10 ms; flip angle = 20°; readout bandwidth = 62.5 kHz; TEs = 2.5, 5.0, and 7.5 ms. The phase encoding gradients were set to shift with the readout for each TE to limit misregistration artifacts from flow. The gradient waveforms were computed by mFast to be as short

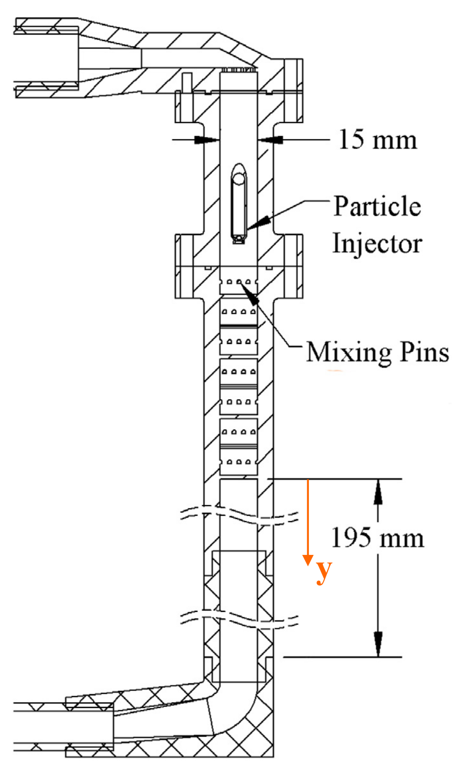

Fig. 1. Schematic of the calibration flow channel. Flow is from top to bottom. Readout was performed in the y direction (labeled).

as possible for the required gradient area given the gradient strength and slew rate limitations of the magnet, which were 50 mT/m and 200 mT/m/s, respectively. The resolution was $0.8 \times 1.0 \times 0.8$ mm in (x, y, z), with readout performed along y, and z (the B_0 axis, L/R in Fig. 1) set as the slice direction. The image matrix was $32 \times 256 \times 34$. To decrease scan time, a cylindrical region of k-space was sampled, omitting the high-frequency corners in the phase encoding plane.

The flow rate and particle loading were controlled independently to produce seven cases: particle volume fractions of 0.10%, 0.21%, 0.42%, and 0.85% at a bulk velocity of 0.42 m/s, and volume fractions of 0.05%, 0.11%, and 0.19% at a bulk velocity of 0.81 m/s. These two velocities correspond to channel Reynolds numbers of 6300 and 12,200. Both are fully turbulent, but turbulent flow fluctuations would be expected over a broader spectrum of length and time scales in the high-*Re* case. Background data were also acquired at the same flow rates with no particles present so that the effect of the particles ($R^*_{2,\mathrm{part}}$) could be isolated from the total decay rate (R^*_2). A total of 6 NEX (short for "Number of EXitations"—equivalent to the number of scans obtained and averaged) were acquired for each of the seven particle/flow conditions, while 20 NEX each were acquired for the two no-particle cases with flow. The multi-NEX data were averaged together for each case to reduce measurement noise due to turbulent fluctuations. The resulting $R^*_{2,\mathrm{part}}$ was computed in each voxel according to the procedure detailed in [25].

3. Results

3.1. Simulations – preferential concentration

Four cases with no particle-fluid slip were simulated: one with a random particle distribution, and three with preferential concentration (at $Stk = 1/4$, 1, and 4). Fig. 2 shows sample particle locations in a central portion of the channel for the four distributions. Mean signal decay rates ($R^*_{2,\mathrm{part}}$) for the baseline case (random distribution) were within 0.3% of the theory for all ϕ_V.

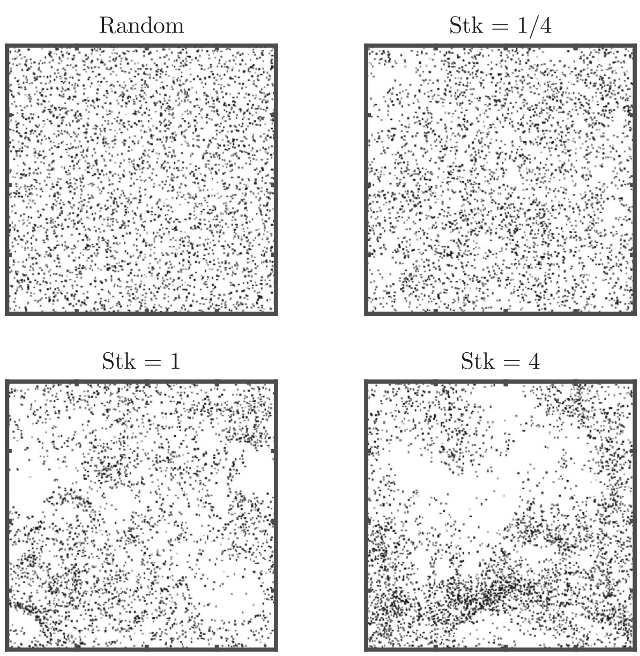

Fig. 2. Example particle positions from a 1/2 mm slice of the simulation domain for the four different particle distributions (L-R, T-B): random, $Stk = 1/4$, $Stk = 1$, and $Stk = 4$. Particle locations were generated from a snapshot of a prior simulation [29].

Fig. 3 shows signal-time curves in a single voxel for the three preferential concentration cases at $\phi_V = 0.4\%$. The three plots show the signal behavior in the voxel with minimum, median, and maximum decay. In all cases, the simulated signal appears to be captured fairly well by an exponential decay model (markers and lines, respectively). However, some minor differences are observable, most notably for the $Stk = 4$ case in the median and maximum decay voxels. For this case, the signal profile is steeper at short TE and shallower at long TE than captured by the exponential model. It is also noteworthy that the variation in signal decay between voxels is much larger at $Stk = 1$ and $Stk = 4$; this reflects the size of the clusters and voids visible in Fig. 2 for those cases.

Fig. 4 shows the signal decay rate for all Stokes numbers and particle concentrations, normalized by the theory value for each ϕ_V. Each marker represents the mean decay rate across all 64 voxels and all four simulations (with different particle distributions), while vertical error bars indicate the 95% confidence interval on the mean. For preferential concentration at $Stk = 1/4$, the decay rate showed only a small decrease. For $Stk = 1$ and 4 a decrease of up to 12% was observed, with the $Stk = 4$ case appearing to show a slightly stronger effect. Also notable is the trend versus ϕ_V, where increasing particle concentration corresponded to a more significant decrease in $R^*_{2,\mathrm{part}}$ at all Stokes numbers.

3.2. Simulations – particle-fluid slip

Simulations were also performed with particle-fluid slip at four slip velocities: 15.6, 23.4, 31.2, and 46.9 mm/s. For reference, the maximum velocity corresponds to motion of around 11 particle diameters during the simulation time. Six slip *angles* were simu-

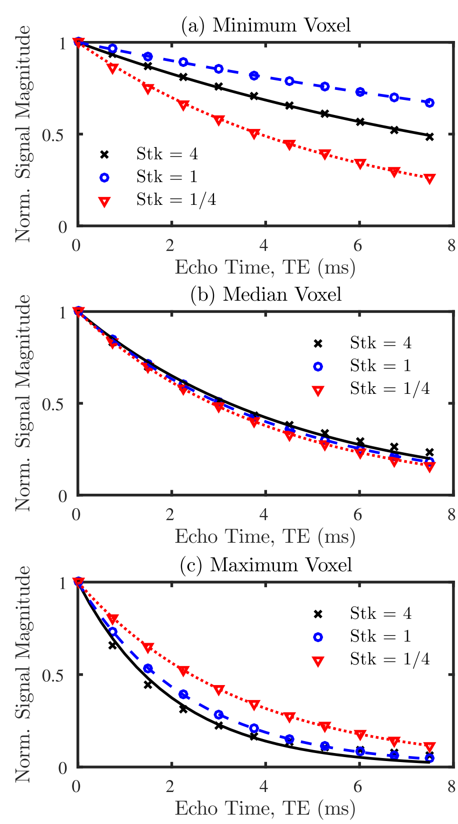

Fig. 3. Signal decay curves for the 0.4% case, with preferential concentration. The three figures are the signal decay in the voxel with the minimum (a), median (b), and maximum (c) signal decay rate for the chosen simulation. Markers indicate the signal magnitude at a given time point, while lines show the best-fit exponential decay curve.

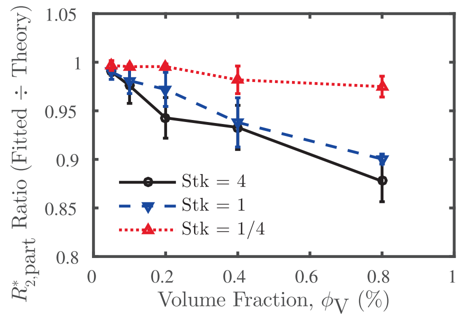

Fig. 4. Normalized $R^*_{2,\mathrm{part}}$, averaged over the entire 64-voxel simulation domain, versus ϕ_V, for cases with preferential concentration. Markers represent the mean values from 4 simulations with different particle locations; vertical error bars show the 95% confidence interval.

lated for each velocity: 0°, 22.5°, 45°, 54.7°, 67.5°, and 90° (0° denotes slip in the B_0 direction). The particle locations were random in all cases with slip.

Both the velocity and direction of particle-fluid slip were found to influence the signal decay curve. Two primary effects were observed. First, high slip velocities tended to produce signal curves that were not monoexponential. Fig. 5 shows signal-time profiles at $\phi_V = 0.4\%$ for voxels with the minimum, median, and maximum decay rates. Results from three slip angles are shown in each plot: 0°, 45°, and 90°. The decay curves appear fairly consistent between the maximum and minimum voxels, which differs from the results observed for the high-Stokes number cases in Fig. 3.

Slip aligned with B_0 produced the most unusual signal behavior. For TE > 3.5 ms, there was negligible loss of signal in any voxel,

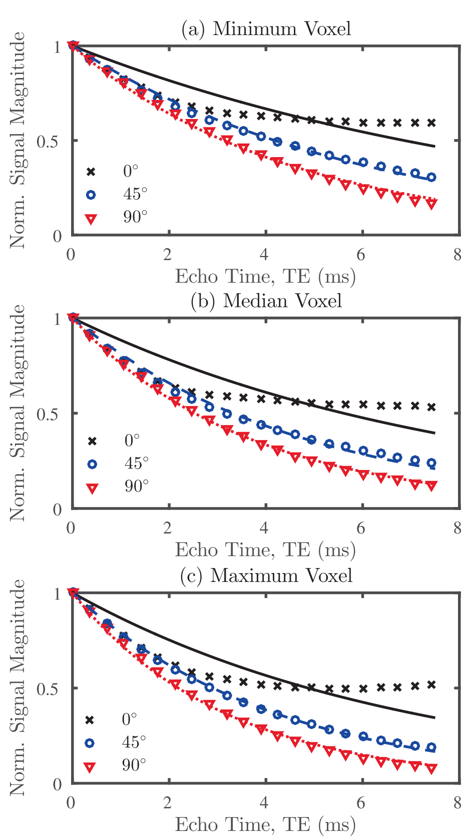

Fig. 5. Signal decay curves for the 0.4% case with particle-fluid slip at 46.9 mm/s. Markers indicate the signal magnitude at a given time point, while lines show the best-fit exponential decay curve.

even though significant signal was still present. For the voxel with maximum decay rate, a slight *increase* in signal can even be observed at long TE. Signal loss also stopped at approximately TE = 6 ms for the 31.2 mm/s case (not shown). Both values correspond to a shift of approximately $5d_p$ between the particles and fluid when signal decay stopped. The resulting signal behavior is not well modeled as an exponential decay process, as evidenced by the poor fit between the simulation data and model curves.

Slip oriented at 45° or perpendicular to B_0 produced less significant changes. Both signal-time curves were roughly exponential, although close examination of the plot shows that the exponential model does deviate slightly. For the 45° case, this deviation has the same sense as at 0° (underprediction of the signal at long TE), while at 90° the trend is reversed, and the exponential curve slightly underpredicts signal at *short* TE. However, these deviations from monoexponential behavior are fairly minor, occurring on the same order of magnitude as with preferential concentration. Fig. 5 also shows that the *initial* slope of the signal-time curves (near TE = 0) was relatively unaffected by slip angle.

Fig. 6 summarizes the measured $R^*_{2,\mathrm{part}}$ versus flow angle at ϕ_V for all four slip velocities simulated. The decay rate is normalized by the appropriate slip velocity (as in Fig. 4). Several trends are apparent. First, slip aligned with B_0 produced a much more pronounced effect on the measured decay rate. As observed in Fig. 5, this discrepancy is due to the signal behavior at long TE for these cases. Second, the effect is relatively nonlinear with slip *velocity*. Doubling the velocity from 23.4 to 46.9 mm/s, for example, changed the measured $R^*_{2,\mathrm{part}}$ value from 95% of theory to only 60% of theory for the 0° case. Finally, there appears to be an angle somewhere between the "magic angle" (54.7°) and 67.5° where the decay rate is unchanged regardless of the slip velocity.

Lastly, Fig. 7 shows the dependence of $R^*_{2,\mathrm{part}}$ on the slip velocity *and* volume fraction for the two most extreme cases: 0° and 90° slip. This figure shows a dependence on ϕ_V in addition to the slip velocity and angle. $R^*_{2,\mathrm{part}}$ was affected most strongly in cases with small ϕ_V. This is the opposite of the trend observed for preferential concentration in Fig. 4, where the largest change occurred at high concentrations.

3.3. Turbulent diffusion

The critical diffusion time, $\tau_{D,\mathrm{crit}}$, was defined earlier as the boundary between the MAR and SDR. For the present particles $\tau_{D,\mathrm{crit}} = 7 \times 10^{-5}$ s, which is 2000× smaller than the actual $\tau_D = 0.14$ s based on molecular diffusivity. The present analysis consists of replacing D with the turbulent diffusion coefficient, D_t, in the definition of τ_D.

Estimating D_t is not straightforward. In this case, it is important to consider that only those turbulent fluctuations occurring on time scales below the maximum TE will manifest as diffusion—larger, slower eddies will produce either uniform particle-fluid slip, as discussed previously, or combined motion of the particles *and* fluid, which should not affect the SDR assumptions. One common estimate for D_t is based on the so-called "mixing length" model [30]:

$$D_t = Sc_t l_m V_T \tag{8}$$

where Sc_t is a dimensionless constant known as the turbulent Schmidt number (typically around 0.9), l_m is a suitable mixing length, and V_T is an estimate for the RMS velocity fluctuations. This model is advantageous because l_m and V_T can be restricted to suitably fast flow fluctuations by requiring that $l_m/V_T < \mathrm{TE}_{\max}$. The ratio $v^3_{\mathrm{eddy}}/l_{\mathrm{eddy}}$ is also constant for all scales of turbulence; thus, D_t can be estimated from any length and velocity scale that correspond

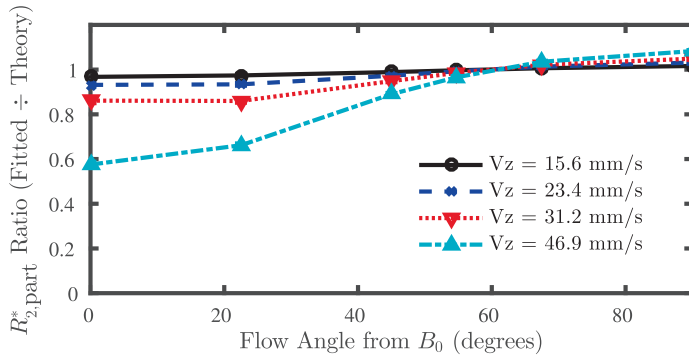

Fig. 6. Normalized $R^*_{2,\mathrm{part}}$, averaged over the entire 64-voxel simulation domain, versus flow angle from B_0. Data shown are from simulations with flow at 46.9 mm/s and $\phi_V = 0.8\%$. Markers represent the mean values from 4 simulations with different particle locations. The 95% confidence interval is smaller than the marker size.

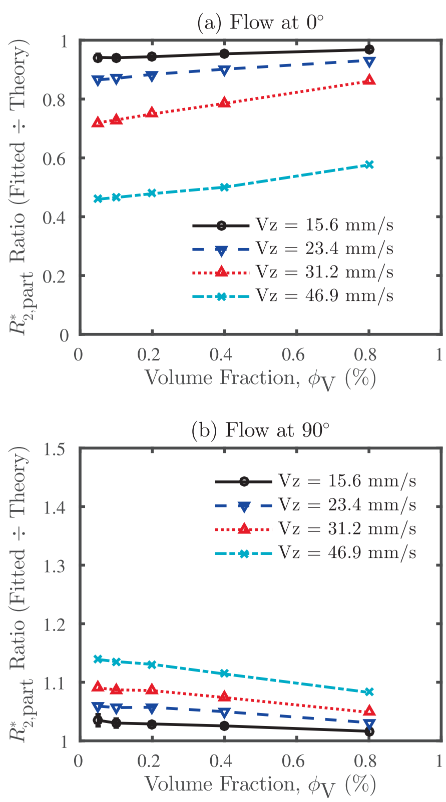

Fig. 7. Normalized $R^*_{2,\mathrm{part}}$, averaged over the entire 64-voxel simulation domain, versus ϕ_V, for cases with particle-fluid slip. Two flow angles are reported: (a) 0° (flow aligned with B_0); (b) 90°. Markers represent the mean values from 4 simulations with different particle locations. The 95% confidence interval is smaller than the marker size.

to a known flow structure. In the main channel U_{bulk} and H are appropriate for large eddies spanning the entire passage, while in the pin wakes $1.5U_{\mathrm{bulk}}$ and w_{pin} are suitable scales for the wake generated by fast flow between the mixing pins.

Table 2 summarizes the results of this analysis for five cases: molecular diffusion (no flow), turbulence in the main channel (at both flow rates), and turbulence in the pin wakes. In the pin wake region, high turbulence levels produce very large D_t values that put the expected behavior in the MAR, with predicted decay rates one or two orders of magnitude lower than the SDR. In the main channel, the estimated τ_D is close to $\tau_{D,\mathrm{crit}}$, which suggests a transitional regime between SDR and MAR; $R^*_{2,\mathrm{part}}$ is expected to decrease by 20% to 80% depending on the Reynolds number.

Table 2
Projected effect of various turbulence levels on $R^*_{2,\mathrm{part}}$.

Flow condition	$D + D_t$ ($\mathrm{m^2/s}$)	τ_D (s)	$\frac{\tau_D}{\tau_{D,\mathrm{crit}}}$	Regime	$\frac{R^*_{2,part}}{R^*_{2,part,SDR}}$
No turbulence	2×10^{-9}	0.14	2000	SDR	1
Main, *Re* 6300	2.0×10^{-6}	1.4×10^{-4}	2.0	Trans.	≈ 0.8
Main, *Re* 12,200	1.4×10^{-5}	1.9×10^{-5}	0.27	Trans.	≈ 0.2
Wake, *Re* 6300	4.4×10^{-5}	6.1×10^{-6}	0.088	MAR	0.083
Wake, *Re* 12,200	3.2×10^{-4}	8.5×10^{-7}	0.012	MAR	0.013

3.4. Flow experiment

Results in the presence of flow showed good agreement with Eq. 1 over most of the measurement domain, but differed in the upstream portion of the channel, near the mixing pins. Fig. 8 shows sample signal-time curves for two regions of the flow: one in the upstream region ($y/H \approx 0.5$), and the other in the channel center ($y/H \approx 8$). In both regions, the signal was averaged over a $4 \times 4 \times 4$ voxel interrogation region (approximately one pin gap width) to provide suitable noise averaging. Vertical error bars showing the 95% confidence interval on mean signal are included, but are approximately the same as the marker size. As in other figures, the lines indicate the best-fit curve using the fitting procedure described in [25].

Although only three data points were available, the fit quality was noticeably better in the channel center versus the upstream region. The error in the upstream fit is most apparent at TE = 2.5 ms, where the decay model overpredicted the signal in all cases; similarly, the model tended to underpredict at 7.5 ms. This effect is similar to the long-TE signal curve flattening observed for the B_0-oriented particle-fluid slip (Fig. 5a). Meanwhile, exponential decay appeared to provide a good description of the data at the channel center.

A plot of the ratio between measured and theoretical decay rates for the experimental data showed significant discrepancies believed to result from uncertainty in the injected ϕ_V, rather than actual changes to $R^*_{2,\mathrm{part}}$. Fig. 9 is presented instead; this figure shows measured $R^*_{2,\mathrm{part}}$ versus ϕ_V for the two interrogation regions. Vertical and horizontal error bars show the 95% confidence interval on the mean decay rate and bulk volume fraction, respectively. The primary source of uncertainty is imperfect knowledge of the bulk ϕ_V. The inset image in each sub-figure is a detailed view showing the high-*Re* case data, while the solid and dashed lines are linear fits to the low- and high-*Re* case data, respectively.

Several trends are apparent from Fig. 9. First, although the $R^*_{2,\mathrm{part}}$ to ϕ_V relationship was relatively linear in all cases, the linear fits predict zero particle decay for $\phi_V \approx 0.02\%$ rather than $\phi_V = 0$. This

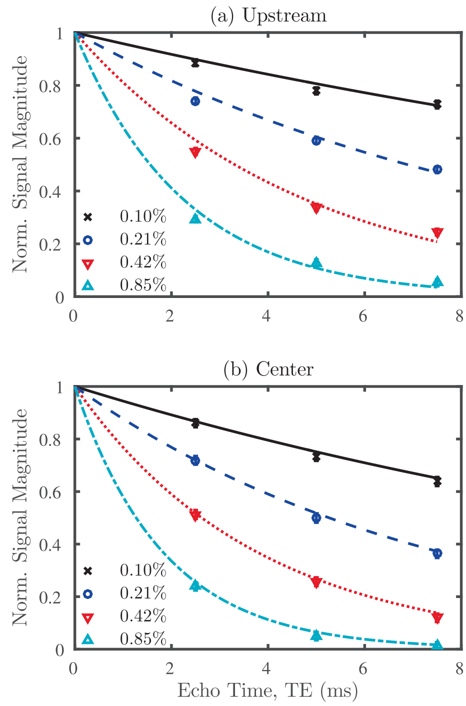

Fig. 8. Average signal intensity in two $4 \times 4 \times 4$ voxel regions of the square channel flow: (a) upstream, near the pins ($y/H \approx 0.5$) and (b) in the center of the imaging region ($y/H \approx 8$). Vertical error bars are mostly within the size of the markers. Solid/dashed curves show the best fit with an exponential decay model.

may have been caused by a small bias in the bulk ϕ_V values achieved during the experiment. However, an alternate explanation is a larger relative reduction in $R^*_{2,\mathrm{part}}$ at low ϕ_V similar to the behavior observed for simulations with slip parallel to B_0 (see Fig. 7b). Second, the calibration curve slopes agreed well with theory (61.4 ms^{-1} per %) in the channel center region, but both slopes were lower than theory in the upstream interrogation region. The high-*Re* case was disproportionately affected: the mean decay rate was about 25% lower than theory, versus 14% lower for the low-*Re* case.

4. Discussion

The simulations and theoretical analysis indicate that preferential concentration, particle–fluid slip, and enhanced diffusion by turbulence may all produce changes to the signal-time curve and measured $R^*_{2,\mathrm{part}}$ versus the expected behavior in the SDR, even when the standard SDR conditions are fulfilled. Each flow phenomenon produces different effects, which may be useful in differentiating between them. The experimental data provide an opportunity to analyze which effects may be important in a realistic flow.

Preferential Concentration. Preferential concentration produced a non-linear reduction in $R^*_{2,\mathrm{part}}$ that depended on the particle concentration and Stokes number. One explanation for the dependence on ϕ_V is that the clusters and voids have little impact on signal loss when particles are spaced far apart, but become important as the particle seeding becomes dense. The Stokes number is known to impact the size and shape of the clusters and voids, so

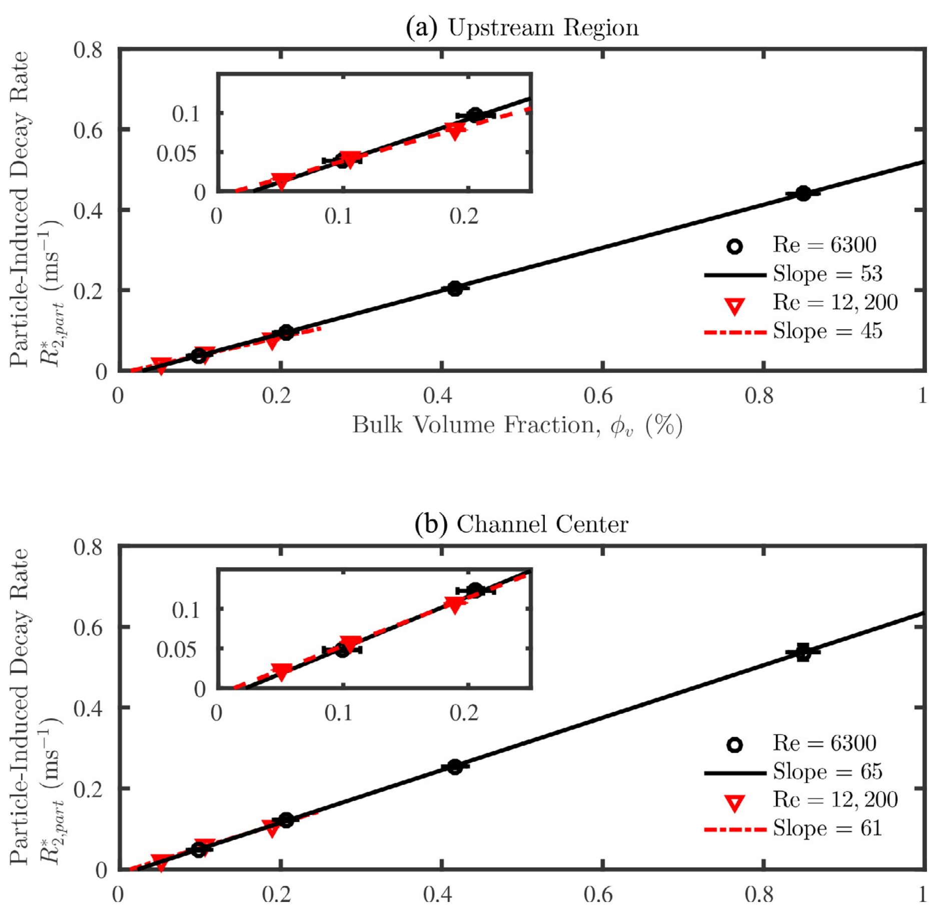

Fig. 9. Signal decay rate, $R^*_{2,\mathrm{part}}$, versus particle concentration, ϕ_V, for all seven experimental cases, averaged over the same two regions as Fig. 8. Inset plots show detail for Re = 12,200 data points.

it is not surprising that it also affected the signal behavior. The standard monoexponential decay model also appeared to perform fairly well, even when $R^*_{2,\mathrm{part}}$ decreased by up to 12%, but some underprediction of the signal value was observed at long TE for the high Stokes number cases. This could be explained by the presence of a large void in a voxel, as the signal in that void would persist much longer than expected for the given bulk ϕ_V.

Preferential concentration was expected at all locations in the experiment based on the estimated Stokes number. Accordingly, one would expect measured $R^*_{2,\mathrm{part}}$ to be lower than SDR theory everywhere in the channel. In reality, $R^*_{2,\mathrm{part}}$ was only lower near the mixing pins. In addition, the experimental calibration curve did not show the disproportionate effect at high concentrations identified in preferential concentration simulations. The experimental data thus did not follow the main trends from the simulations; however, it is difficult to gauge the reliability of these comparisons as the exact structure of clusters and voids in a real flow depends on factors beyond the Stokes number alone.

Particle-Fluid Slip. In the presence of particle-fluid slip, each proton will experience both positive and negative magnetic field disturbances as it travels past nearby particles. This process is similar to fast diffusion, so one might expect a reduction in $R^*_{2,\mathrm{part}}$ similar to the transition from the SDR to the MAR. However, the present simulations showed very different behavior in which the signal-time curve was no longer monoexponential.

For slip parallel to B_0, the signal became essentially constant at long echo times. The time at which the curve became flat varied with the slip velocity, but generally corresponded to a net motion of around 5 particle diameters. This result suggests that the total particle displacement within one TE plays an important role. Because of the strongly non-exponential shape of the signal curve, the $R^*_{2,\mathrm{part}}$ computed by fitting an exponential decay model was much lower than the theoretical value. Slip perpendicular to B_0 led to slightly *increased* $R^*_{2,\mathrm{part}}$ and slip occurring at around 60° produced almost no effect. The signal curves in these cases were fairly well-represented by an exponential decay model.

The initial portion of the signal-time curves showed very little dependence on the slip velocity and angle. This is an important result as it suggests any effects of slip could be mitigated by scanning at shorter TE. Unfortunately, reducing TE also reduces sensitivity to the particles as less decay occurs, so the two effects would need to be balanced appropriately. It is also interesting to note that the effects of slip appear more pronounced at *low* ϕ_V. This was the opposite of the trend due to preferential concentration and offers some possibility for distinguishing the two effects.

In the experiment, particle-fluid slip likely occurred in all directions and with fluctuations in time. It is difficult to make any claims regarding the actual distribution of velocities, but it may be reasonable to assume there was, at most, a weak directional preference given the complexity of flow behind rows of perpendicular pins. Meanwhile, slip aligned with B_0 was shown to produce a disproportionately large effect on $R^*_{2,\mathrm{part}}$ in the simulations. Thus, it seems plausible that the net effect for flow with a near-isotropic distribution of slip velocities would be a flattening of the signal curve at longer echo times and reduction of measured $R^*_{2,\mathrm{part}}$.[1] Particle-fluid slip could therefore explain the non-exponential behavior suggested by Fig. 8a, as well as the calibration curve in Fig. 9a, which shows a larger relative decrease in $R^*_{2,\mathrm{part}}$ at low ϕ_V. Although they were not necessarily representative of the actual conditions in the experiment, the simulations with slip produced results that were most consistent with the experimental data.

Turbulent Diffusion. The effect of turbulent diffusion was examined using standard MRI relaxation theory. However, this analysis predicted $R^*_{2,\mathrm{part}}$ values far below those measured in the channel. One explanation for the discrepancy is that the analysis assumed turbulent diffusion acting around *stationary* particles. In reality, the particles generally move with the fluid, including many of the turbulent fluctuations that disperse water molecules. An additional possibility is the variation of apparent D_t with echo time described in [28]. However, the present analysis was based on restricting the D_t estimate to eddies with a turnover time less than the maximum TE, which is based on similar physical principles. Moreover, the entire analysis (including that reviewed in [28]) assumes homogeneous turbulence, which is unlikely in the pin wake region. Overall, any effect from turbulent diffusion of protons appears to be coupled to the particle-fluid slip, invalidating the simple analysis attempted here.

Future Work. A primary limitation of the present work was lack of knowledge regarding the distribution of particle positions and velocities in the experimental flow. This prohibited a quantitative comparison between the simulations and experimental measurements, since the flow conditions could not be matched reliably. Both experimental and computational approaches could be considered to address this disconnect; however, a high-fidelity simulation appears more feasible given the difficulty of laser-based measurements at the particle volume fractions of interest. In either case, such work is beyond the scope of the present study and is left as a recommendation for future research.

In addition, further mathematical treatment of these flow-related phenomena could be undertaken using the present simulation results as a guide. The effects of unidirectional slip, in particular, might be investigated by considering line integrals along various trajectories to explain the disproportionate effect of slip aligned with B_0. The signal phase is also known to change in the presence of particles; phase information was not used in the experiments due to the effects of phase drift, but phase values were computed in the simulation results and could be used for further investigation of the effects of slip or preferential concentration.

5. Conclusions

The MRP method is a promising new tool for biological and non-biological studies. One limitation of MRP to date has been a discrepancy between the measured $R^*_{2,\mathrm{part}}$ and predictions using SDR theory in some regions of flow, which affects confidence in the measurements. Simulation were carried out to show that the SPGR signal is likely sensitive to two common particle-laden flow phenomena. Preferential concentration was shown to cause reduction in $R^*_{2,\mathrm{part}}$ while only weakly affecting the monoexponential shape of the signal decay curve. The $R^*_{2,\mathrm{part}}$ effect was more pronounced at larger ϕ_V. Uniform particle-fluid slip produced non-exponential behavior in the signal-time curve with a significant dependence on the slip orientation (relative to B_0) and velocity. Slip aligned with B_0 produced the strongest effect: flattening of the signal curve at long TE, and a corresponding reduction in the $R^*_{2,\mathrm{part}}$ measured by fitting a monoexponential decay curve.

A theoretical analysis suggested that turbulent diffusion around stationary particles could cause order-of-magnitude or larger decreases in $R^*_{2,\mathrm{part}}$ for the flow conditions in the experimental channel, based on existing relaxation theory. However, this decrease was not observed in the experimental data, indicating that the analysis was too limited in scope to describe a realistic flow. The combined results from simulations, theory, and experiment suggest that particle-fluid slip was most likely the mecha-

[1] This is true even accounting for the existence of two directions perpendicular to B_0 vs. one parallel—an integral of the curves in Fig. 6 in spherical coordinates, with the horizontal axis used as the polar angle, produces a value less than a corresponding integral of 1.

nism behind the discrepancy between the experimental data and SDR theory near the mixing pins. However, it should be noted that the simulations were not designed to replicate the experimental flow conditions, and that additional nonidealities and other flow effects, such as modification of the turbulence by particles, were not considered.

Declaration of Competing Interest

The authors declare that there is no conflict of interest.

Acknowledgements

Funding: This work was supported by a National Science Foundation Fluid Dynamics EAGER award [Grant CBET-1662422] and a pilot grant from the Richard M. Lucas Center for Imaging at Stanford University. Daniel Borup was supported by an NSF Graduate Research Fellowship [Grant DGE-114747] and an Office of Technology Licensing Stanford Graduate Fellowship. The authors are also grateful to Prof. John Dabiri for suggesting a detailed analysis of particle-fluid slip, and to Prof. Brian Hargreaves for several insightful conversations during the development of MRP.

Appendix A. Simulation methodology

The simulation code was written using Matlab software (MathWorks, Inc.). The same code was used for all simulations; the code allowed for the various conditions described in the Methods section to be enforced as desired. The algorithm was as follows.

First, to begin each simulation, a 3D computational mesh was initialized. The domain consisted of a triply periodic $4 \times 4 \times 4$ mm cube representing a $4 \times 4 \times 4$ array of 1 mm^3 measurement voxels, similar to the experiment. Within this domain, magnetization vectors of unit magnitude and zero phase were initialized on an isotropic Cartesian grid with N points per millimeter, where N could be varied. The impact of mesh refinement was assessed by running the baseline case at $N = 32$, 64, 96, and 128, and comparing the results to SDR theory (Eq. (1)). $N = 96$ was chosen for remaining simulations as the mean decay rate across all voxels (after 4 repetitions) was within 0.3% of theory at all ϕ_V.

Particle locations were initialized independently from the grid of magnetization vectors — the particle locations were stored as a separate data array of float values. For cases with preferential concentration, locations were generated from a snapshot of a computational fluid dynamics (CFD) simulation of particle-laden homogeneous, isotropic turbulence (HIT) in a triply periodic box [29]. The CFD domain was dimensionless, with units of Kolmogorov lengths; accordingly, an arbitrary cubic sub-domain of 307η was chosen to achieve the correct length scaling, based on the estimated $\eta = 13$ μm in the experiment.

After selecting and scaling the sub-domain, the algorithm consisted of choosing particles randomly from the CFD snapshot. For each new particle choice, the distance to all previous particles was computed. If any other particle was within $d_p = 33$ μm, the new particle was discarded; otherwise its location was saved and the process repeated until the required ϕ_V had been reached. Individual voxels were allowed to vary in concentration; the target ϕ_V was enforced only over the entire domain. This was necessary to preserve the preferential concentration structures, which often had sizes on the order of the voxel width. For cases *without* preferential concentration, locations were generated by simply choosing random numbers for the three coordinates, then proceeding with collision checking as above.

Once particle locations had been initialized, the resulting magnetic field disturbance was solved on the magnetization vector grid. To reduce computation time, the disturbance from each particle was computed only inside the smallest cube across which it would produce up to 0.01 radians of phase accumulation during the entire simulation. Each disturbance map was saved with the corresponding particle locations for re-use (e.g. for cases at different slip velocities).

The magnetization simulation proceeded as a set of discrete forward time steps, with interval Δt, until the maximum echo time (7.5 ms) was reached. For static simulations, Δt was capped at 0.25 ms. For simulations with slip, Δt was capped at the smaller of 0.25 ms or the time for a particle to move 1/4 of the grid spacing. For each time step, the magnetic field disturbance was recomputed by linear interpolation from the initial map based on the appropriate linear shift—in essence, the particle locations remained fixed and the grid of magnetization vectors was shifted. Linear interpolation was used to lower computation time, as solving for the full field map was computationally intensive. Next, the phase of each magnetization vector was updated according to $\gamma \cdot \Delta B \cdot \Delta t$ (i.e., the spin phases were tracked after demodulation by B_0). Lastly, the signal was averaged over all N^3 grid points in each 1 mm^3 voxel to produce an instantaneous signal at the MRI measurement scale.

This process was repeated to examine all of the cases listed in Table 1. For each particle volume fraction and distribution type (random and Stk = 1/4, 1 and 4), four sets of particle locations and their resulting field disturbance maps were generated and saved. The simulations were then repeated four times using the four particle location sets to provide information on uncertainty due to the specific choice of particle locations. The same set of four random particle locations at a given ϕ_V were used for all cases with slip to improve consistency of results across the different velocities and angles. The full set of simulations took approximately 5 days to run on a Linux workstation with 8 processor cores and 24 GB of RAM.

It should be noted that the simulation required some simplifications versus a real-world scenario. Longitudinal magnetization, relaxation, and RF effects were not considered. The simulations also did not include any nonidealities introduced by phase encoding or readout gradients. The results represent the signal that would be measured given an instantaneous sampling of all of k-space immediately after an ideal 90 degree excitation.

References

[1] M. Salerno, C.M. Kramer, Advances in parametric mapping with cmr imaging, JACC: Cardiovasc. Imag. 6 (2013) 806–822.
[2] J.C. Wood, Magnetic resonance imaging measurement of iron overload, Curr. Opin. Hematol. 14 (2007) 183.
[3] D.R. Messroghli, J.C. Moon, V.M. Ferreira, L. Grosse-Wortmann, T. He, P. Kellman, J. Mascherbauer, R. Nezafat, M. Salerno, E.B. Schelbert, et al., Clinical recommendations for cardiovascular magnetic resonance mapping of t1, t2, t2∗ and extracellular volume: a consensus statement by the society for cardiovascular magnetic resonance (scmr) endorsed by the european association for cardiovascular imaging (eacvi), J. Cardiovasc. Magn. Reson. 19 (2017) 75.
[4] S. Ogawa, T.-M. Lee, A.R. Kay, D.W. Tank, Brain magnetic resonance imaging with contrast dependent on blood oxygenation, Proc. Natl. Acad. Sci. 87 (1990) 9868–9872.
[5] Y.-X.J. Wang, S.M. Hussain, G.P. Krestin, Superparamagnetic iron oxide contrast agents: physicochemical characteristics and applications in mr imaging, Eur. Radiol. 11 (2001) 2319–2331.
[6] D.O. Kuethe, Measuring distributions of diffusivity in turbulent fluids with magnetic-resonance imaging, Phys. Rev. A 40 (1989) 4542.
[7] J. Gatenby, J. Gore, Mapping of turbulent intensity by magnetic resonance imaging, J. Magn. Reson., Ser. B 104 (1994) 119–126.
[8] T.-Q. Li, J.D. Seymour, R.L. Powell, K.L. McCarthy, L. Ödberg, M.J. McCarthy, Turbulent pipe flow studied by time-averaged nmr imaging: measurements of velocity profile and turbulent intensity, Magn. Reson. Imag. 12 (1994) 923–934.
[9] P. Dyverfeldt, R. Gårdhagen, A. Sigfridsson, M. Karlsson, T. Ebbers, On mri turbulence quantification, Magn. Reson. Imag. 27 (2009) 913–922.

[10] M. Markl, S. Schnell, C. Wu, E. Bollache, K. Jarvis, A.J. Barker, J.D. Robinson, C.K. Rigsby, Advanced flow mri: emerging techniques and applications, Clin. Radiol. 71 (2016) 779–795.
[11] K.J. Ryan, F. Coletti, C.J. Elkins, J.O. Dabiri, J.K. Eaton, Three-dimensional flow field around and downstream of a subscale model rotating vertical axis wind turbine, Exp. Fluids 57 (2016) 38.
[12] M. Sankey, D. Holland, A. Sederman, L. Gladden, Magnetic resonance velocity imaging of liquid and gas two-phase flow in packed beds, J. Magn. Reson. 196 (2009) 142–148.
[13] K.J. Ryan, J. Bodart, M. Folkersma, C.J. Elkins, J.K. Eaton, Turbulent scalar mixing in a skewed jet in crossflow: experiments and modeling, Flow, Turbul. Combust. 98 (2017) 781–801.
[14] J.F. Schenck, The role of magnetic susceptibility in magnetic resonance imaging: MRI magnetic compatibility of the first and second kinds, Med. Phys. 23 (1996) 815–850.
[15] H.W. de Haan, Mechanisms of proton spin dephasing in a system of magnetic particles, Magn. Reson. Med. 66 (2011) 1748–1758.
[16] R.J. Brown, Distribution of fields from randomly placed dipoles: free-precession signal decay as result of magnetic grains, Phys. Rev. 121 (1961) 1379.
[17] D. Yablonskiy, E.M. Haacke, Theory of NMR signal behavior in magnetically inhomogeneous tissues: the static dephasing regime, Magn. Reson. Med. 32 (1994) 749–763.
[18] R.A. Brooks, F. Moiny, P. Gillis, On t2-shortening by weakly magnetized particles: the chemical exchange model, Magn. Reson. Med.: An Off. J. Int. Soc. Magn. Reson. Med. 45 (2001) 1014–1020.
[19] A.L. Sukstanskii, D.A. Yablonskiy, Effects of restricted diffusion on mr signal formation, J. Magn. Reson. 157 (2002) 92–105.
[20] C.M. Sandino, P. Kellman, A.E. Arai, M.S. Hansen, H. Xue, Myocardial t2$*$ mapping: influence of noise on accuracy and precision, J. Cardiovasc. Magn. Reson. 17 (2015) 7.
[21] P. Hardy, R. Henkelman, Transverse relaxation rate enhancement caused by magnetic particulates, Magn. Reson. Imag. 7 (1989) 265–275.
[22] R.N. Muller, P. Gillis, F. Moiny, A. Roch, Transverse relaxivity of particulate mri contrast media: from theories to experiments, Magn. Reson. Med. 22 (1991) 178–182.
[23] R. Weisskoff, C.S. Zuo, J.L. Boxerman, B.R. Rosen, Microscopic susceptibility variation and transverse relaxation: theory and experiment, Magn. Reson. Med. 31 (1994) 601–610.
[24] R. Wessel, J. Righi, Generalized correlations for inertial impaction of particles on a circular cylinder, Aerosol. Sci. Technol. 9 (1988) 29–60.
[25] D.D. Borup, C.J. Elkins, J.K. Eaton, Development and validation of an mri-based method for 3d particle concentration measurement, Int. J. Heat Fluid Flow 71 (2018) 275–287.
[26] D.D. Borup, C.J. Elkins, J.K. Eaton, Transport of microparticles in a turbulated serpentine passage, in: ASME Turbo Expo 2017: Turbomachinery Technical Conference and Exposition, American Society of Mechanical Engineers, 2017, Paper number 63491.
[27] D.D. Borup, L.E. Engel, C.J. Elkins, J.K. Eaton, Transport and Dispersion of Particle-Laden Streaks in a Standardized Human Nasal Geometry, in: 19th International Symposium on Applications of Laser Techniques to Fluid Mechanics.
[28] D.O. Kuethe, J.-H. Gao, Nmr signal loss from turbulence: models of time dependence compared with data, Phys. Rev. E 51 (1995) 3252.
[29] A.J. Banko, L. Villafane, J.H. Kim, M. Esmaily, J.K. Eaton, Stochastic modeling of direct radiation transmission in particle-laden turbulent flow, J. Quant. Spectrosc. Radiat. Transf. 226 (2019) 1–18.
[30] P. Davidson, Turbulence: An Introduction for Scientists and Engineers, Oxford University Press, 2015.